Development of a Dynamic Decohesion Criterion for Subsonic Fracture of the Interface between Two Dissimilar Materials

Author(s): John Lambros and Ares J. Rosakis

Source: *Proceedings: Mathematical and Physical Sciences*, Vol. 451, No. 1943 (Dec. 8, 1995), pp. 711-736
Published by: Royal Society
Stable URL: https://www.jstor.org/stable/52746
Accessed: 06-07-2022 04:20 UTC

Development of a dynamic decohesion criterion for subsonic fracture of the interface between two dissimilar materials

By John Lambros† and Ares J. Rosakis

Graduate Aeronautical Laboratories, California Institute of Technology, Pasadena, CA 91125, USA

We present findings of an experimental study of dynamic decohesion of bimaterial systems composed of constituents with a large material property mismatch. Poly-methylmethacrylate (PMMA)–steel and PMMA–aluminium bimaterial fracture specimens were used. Dynamic one-point bend loading was accomplished with a drop-weight tower device (for low and intermediate loading rates) or a high-speed gas gun (for high loading rates). High-speed interferometric measurements were made using the lateral shearing interferometer of coherent gradient sensing in conjunction with high-speed photography. Very high crack propagation speeds (terminal crack-tip speeds up to $1.5c_s^{PMMA}$, where c_s^{PMMA} is the shear wave speed of PMMA) and high accelerations (of about $10^7 g$, where g is the acceleration of gravity) were observed and are reported. Issues regarding data analysis of the high-speed interferograms are discussed. The effects of near-tip three-dimensionality are also analysed. Dynamic complex stress factor histories are obtained by fitting the experimental data to available asymptotic crack-tip fields. A dynamic crack growth criterion for crack growth along bimaterial interfaces is proposed. In the subsonic regime of crack growth it is seen that the opening and shearing displacements behind the propagating crack tip remain constant and equal to their value at initiation, i.e. the crack retains a self-similar profile during crack growth at any speed. This forms the basis of the proposed dynamic interfacial fracture criterion.

1. Introduction

In the past 10 years there has been considerable interest in investigating phenomena associated with interfacial fracture. Research on this topic has been mostly analytical in nature and has been confined to situations of quasi-static loading and slow crack growth. From the pioneering work of Williams (1959) to more recent contributions (Rice 1988; Shih 1991), it has been seen that the stresses near the tip of a crack between two dissimilar linear elastic solids exhibit a pathological singularity of an oscillatory nature as the tip is approached. In addition, the predicted crack-face displacements are seen to exhibit crack-face contact. It is now clear that such a behaviour is an artifact of the assumptions of linear elasticity. When the inter-

† Present address: Mechanical Engineering Department, University of Delaware, Newark, DE 19716, USA.

Proc. R. Soc. Lond. A (1995) **451**, 711–736
Printed in Great Britain

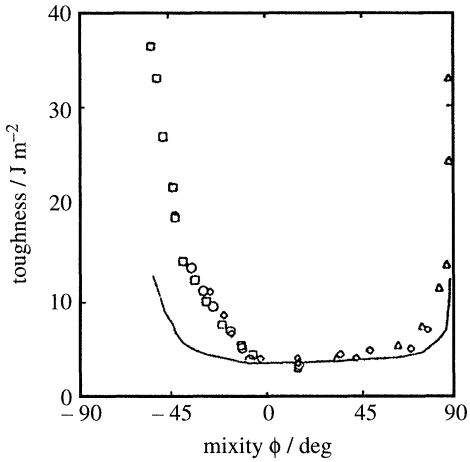

Figure 1. Quasi-static interfacial toughness of glass–epoxy system. ○ test 1; □ test 2; ◇ test 3; △ test 4; — predicted toughness. (From Leichti & Chai 1992.)

face constituents are modelled as fully nonlinear neo-Hookean hyperelastic solids, the pathologies of all interfacial stress and displacement fields disappear. This was shown by the analytical contributions of Knowles & Sternberg (1983) and Geubelle & Knauss (1994*a*, *b*). Similar conclusions are reached when plasticity is allowed to develop in the vicinity of the interfacial crack-tip (Shih & Asaro 1988, 1989; Shih *et al.* 1991).

Several experimental studies of interfacial fracture have been reported, though considerably fewer than analytical ones. However, the majority of experimental research on this subject involves problems that are quasi-static in nature. Driven by experimental observations, a criterion for quasi-static interfacial crack initiation and growth has been proposed by Liechti & Chai (1991). This involves a relation between the energy release rate G and the phase angle ϕ of the type shown in figure 1. When near-tip deformations are K-dominant, the above criterion is equivalent to the results of Liechti & Knauss (1982*a*, *b*) who observed that quasi-static interfacial crack growth in polymer–glass interfaces proceeds under constant vectorial crack-face displacement.

To fully understand the catastrophic nature of interfacial fracture, a detailed investigation of dynamic interfacial fracture mechanics is necessary. Due to the complexity of this problem, however, only a few theoretical investigations have been made so far (Goldshtein 1967; Brock & Achenbach 1973; Willis 1971, 1973; Atkinson 1977; Yang *et al.* 1991; Deng 1993). To our knowledge, only a experimental study on this subject is currently available (Tippur & Rosakis 1991).

Here, we investigate the essentially unexplored area of experimental dynamic interfacial fracture mechanics. In particular, in the context of the present paper, it is intended to obtain a physically based and accurate criterion for dynamic crack initiation and growth in bimaterial systems. The use of high-speed photography and interferometric optical diagnostics provides real-time measurements of the mechanical fields in the vicinity of the initiating and propagating interfacial crack tip. The particular optical method used in this study is the newly developed method of coherent gradient sensing (CGS) (Tippur *et al.* 1991; Rosakis 1993). This is a full-field lateral shearing interferometer which has shown great promise in real-time imaging

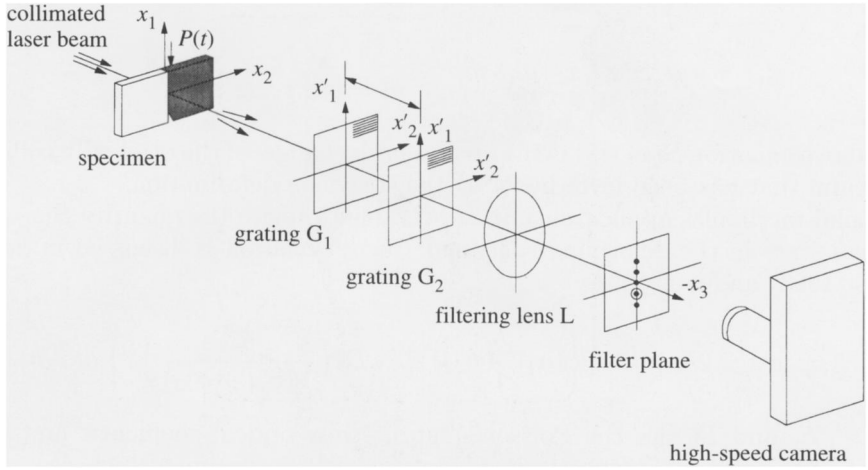

Figure 2. Schematic of CGS setup in transmission.

of dynamic crack-tip fields in homogeneous materials. The optical interferograms obtained from this technique are analysed using theoretically predicted near-tip stress fields (Liu *et al.* 1993). The results are then used to formulate and propose a criterion for dynamic crack initiation and growth along bimaterial interfaces.

2. Experimental procedure

(*a*) *Coherent gradient sensing interferometer (CGS)*

The physical principle governing the method of CGS was first analysed by Tippur *et al.* (1991) and is described in detail by Rosakis (1993). Figure 2 is a schematic of the CGS arrangement in a transmission configuration. The bimaterial specimen configuration shown is composed of a poly-methylmethacrylate (PMMA)–metal combination. A coherent, monochromatic, collimated laser beam is incident on the deforming specimen. After transmission through the transparent (PMMA) side of the specimen, it acquires an optical path difference and looses collimation. The optical path difference acquired is due to stress induced differences in refractive index and due to a non uniform contraction in the thickness direction around the vicinity of the crack-tip (Poisson's ratio effect). The resulting, now non-collimated, beam passes through two line diffraction gratings G_1 and G_2 of fine pitch p. They are situated a distance Δ apart and perform a shearing of the incident wave front. The gratings' output intensity is transmitted through a filtering lens L. A diffraction spot pattern is obtained on the filtering plane, which is located at the back focal plane of lens L. At this plane, all but one diffraction orders are blocked. The one remaining diffraction spot (either of ± 1 orders), shown in figure 2 as the open circle on the filtering plane, is imaged to produce an interference pattern. For the case of a dynamic experiment the imaging device is a high-speed camera focused on the specimen.

For the sake of simplicity and brevity we will not present the details of analysing the CGS optical method. These details can be found in several older articles including Tippur *et al.* (1991) and Rosakis (1993). In addition a more rigorous derivation of the CGS interferometric formulas can be found in Tippur (1992) and Lee *et al.* (1995). The condition for the formation of constructive interference CGS fringes on the image

plane is

$$\frac{\partial\left(S(x_1, x_2)\right)}{\partial x_1} = \frac{mp}{\Delta}, \quad m = 0, \pm 1, \pm 2, \ldots \tag{1}$$

In the above equation $S(x_1, x_2)$ is the optical path change, of the originally collimated laser beam, that has been introduced by the specimen deformation.

For solid mechanics applications, it is desirable to relate the quantity $S(x_1, x_2)$ to the stress state in the deforming specimen. Such a relation is discussed in detail in Rosakis (1993) and is given by:

$$S(x_1, x_2) = 2hc_\sigma \int_0^{1/2} \left\{ (\sigma_{11} + \sigma_{22}) \left[1 - D_2 \left(\frac{\sigma_{33}}{\nu(\sigma_{11} + \sigma_{22})} \right) \right] \right\} \mathrm{d}(x_3 h) \tag{2}$$

where ν , c_σ and D_2 are the Poisson's ratio, stress optical coefficient and optical constant of the material respectively. Quantity h is the specimen thickness.

(*b*) *Effects of three-dimensionality on data analysis*

The discussion of the previous section was intentionally kept as general as possible within the assumptions of isotropic linear elasticity. For either a homogeneous or a bimaterial cracked linear elastic plate of uniform thickness and finite in-plane dimensions, the optical path difference S acquired by light transmission through the specimen thickness will in general depend on the details of the three-dimensional elastostatic or elastodynamic stress state that would exist at the vicinity of the crack-tip. It will be a function of the applied loading, as well as of the in-plane dimensions and thickness of the specimen. For a bimaterial system it is also expected to depend on the material mismatch.

Given the lack of full-field, three-dimensional analytical solutions in fracture mechanics, experimental information can strictly be extracted by means of detailed numerical calculations. Nevertheless, there exist certain non-trivial special cases for which available asymptotic solutions, based on two-dimensional analyses, may provide adequate approximations for $S(x_1, x_2)$ at certain regions near the crack-tip.

To illustrate the extent of the near-tip three-dimensionality in a cracked bimaterial interface, reference is made to figure 3 which shows a three-dimensional representation of the ratio $\sigma_{33}/\nu(\sigma_{11} + \sigma_{22})$ for a pre-cracked three-point bend PMMA–aluminium bimaterial specimen. This is the same quantity that appears in the second term of the integrand of the optical path change relation in (2). The above ratio is often called the degree of plane strain. It is a measure of near-tip three-dimensionality and has been obtained by means of a three-dimensional finite-element calculation which models a stationary crack in a three-point bend bimaterial specimen subjected to dynamic loading. In figure 3, only the PMMA side of the bond is illustrated. In regions where the deformation is locally plane stress, this measure equals zero (i.e. $\sigma_{33} = 0$). When the deformation approaches plane strain-like conditions, the ratio approaches one (i.e. $\sigma_{33} = \nu(\sigma_{11} + \sigma_{22})$). The top surface visible in the figure corresponds to the mid-plane of the specimen. The traction-free crack surface is on the left-hand side of the picture. It is clear that there exists a substantial region of three-dimensional deformation that extends along the bond line. The width of this band is approximately equal to half the specimen thickness. However, it is also evident that there exists a wedge of plane stress conditions defined by $100° < \theta < 150°$ and down to $r \approx 0.2h$. The cylindrical coordinate system (r, θ, x_3) is centered at the crack front

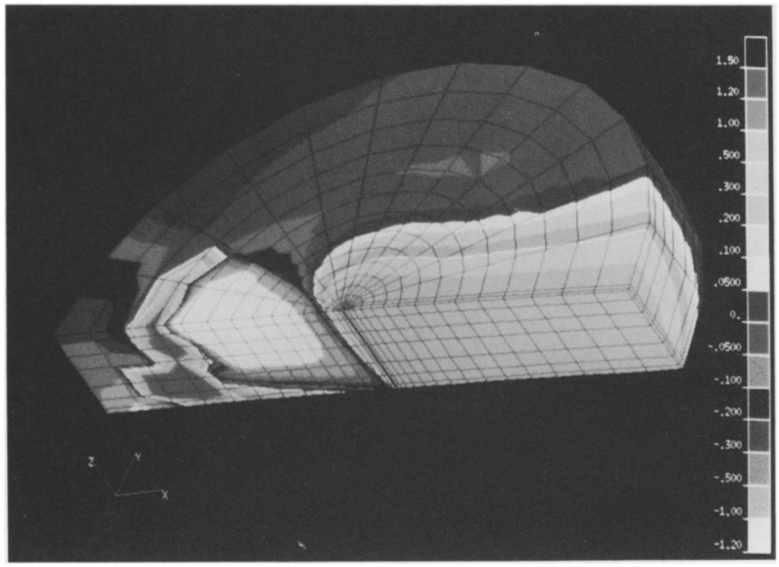

Figure 3. Contours of numerically calculated degree of plane strain in a dynamically loaded bimaterial cracked plate.

and h is the specimen thickness. (For more details on the numerical analysis leading to this result, see Lee & Rosakis (1993).)

We can now use the results of the numerical computation when interpreting optical patterns using (2). If we choose to analyse only points outside the three-dimensional region, in the region of plane stress conditions, then the optical path difference S in (2) will simplify to

$$S(x_1, x_2) \approx c_\sigma h \left[\hat{\sigma}_{11}(x_1, x_2) + \hat{\sigma}_{22}(x_1, x_2)\right], \tag{3}$$

where $\hat{\sigma}_{11}$ and $\hat{\sigma}_{22}$ are *thickness averages* of the in-plane stress components in the plate.

Thus, for points outside the near-tip three-dimensional region the CGS patterns assume a simple interpretation in terms of two-dimensional stress field approximations. In particular, (1) in conjunction with (3) now indicates that the fringes obtained from regions surrounding the three-dimensional zone can be related to the in-plane gradient component of $\hat{\sigma}_{11} + \hat{\sigma}_{22}$ as follows:

$$c_\sigma h \frac{\partial(\hat{\sigma}_{11} + \hat{\sigma}_{22})}{\partial x_1} = \frac{mp}{\Delta}, \quad m = 0, \pm 1, \pm 2, \ldots, \tag{4}$$

where in the case of transmission c_σ is the stress optical coefficient of PMMA.

(*c*) *Bimaterial experiments*

In order to intensify dynamic effects at the interface, it was decided to use bimaterial constituents that have a very large mechanical property mismatch. This would allow us to investigate easier the more extreme cases of interfacial behaviour. To be able to use a transmission CGS arrangement in our experimentation, one side of the bond, the more compliant side, was chosen to be PMMA. This is a transparent polymer that is easily machined and handled. At room temperature it behaves in a brittle fashion. The other side of the bond was chosen as either 6061-T6 aluminium

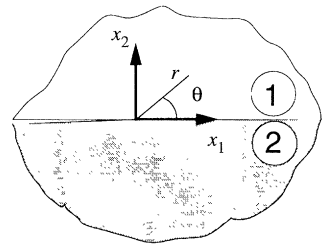

Figure 4. Geometry of interfacial crack problem.

Table 1. *Mechanical properties of interface constituents*

property	PMMA	6061-T6 aluminium	AISI 4340 steel
E/GPa	3.24	80	208
v	0.35	0.33	0.3
$c_d/(\mathrm{m\ s^{-1}})$	2080	6600	5970
$c_s/(\mathrm{m\ s^{-1}})$	1000	3330	3190
$c_R/(\mathrm{m\ s^{-1}})$	935	3100	2950
$\rho/(\mathrm{kg\ m^{-3}})$	1190	2710	7830
$\varepsilon^{P/A} = 0.0981$		$\varepsilon^{P/S} = 0.1037$	$\varepsilon^{P/R} = 0.1073$

or AISI 4340 steel, both of which are considerably stiffer and tougher than PMMA. They also have wave speeds which are considerably larger than those in polymers. Throughout this study, the PMMA side of each specimen will be referred to as material 1 and the metal side as material 2. So with reference to figure 4, the more compliant material occupies the positive x_2 plane. The mechanical properties of the constituents are shown in table 1.

The specimen preparation procedure follows the lines of Tippur & Rosakis (1991). For the precise details of the bonding procedure, the reader can refer to this work. However, an issue that is of importance, and should be discussed here, is the issue of bond strength. Bond strength estimation has been addressed by the performance of bond calibration tests by Tippur & Rosakis (1991). Their method essentially consists of a static test to measure the fracture toughness of a specimen made up of two halves of PMMA bonded together. It was shown there that the fracture toughness of the bonded PMMA specimens was over 95% of that of homogeneous PMMA. Therefore, the adopted bonding procedure results in a PMMA–PMMA specimen whose stiffness and toughness characteristics are almost exactly those of homogeneous PMMA. Additional quasi-static crack growth tests in PMMA–steel three-point bend edge cracked plates were performed in the context of the present work. In these experiments it was seen that the minimum measured quasi-static initiation toughness (corresponding to a primarily opening mode of crack initiation) was again about 95% of the toughness of homogeneous PMMA.

In the experiments described in the next two sections, bimaterial fracture specimens containing either a blunt notch or a sharp pre-crack along the interface were used. After being bonded, a starter notch was machined in the specimen using a band saw. In all cases the notch was cut along the interface. Care was taken to cut equally

into the PMMA and metal sides of the bond. A slow cut speed insured no or very little residual stresses in the PMMA. The length of the starter notch in all cases was 25 mm. The width of the notch, which was dictated by the width of the band saw blade, was approximately 750 μm. In some experiments, a sharp pre-crack was used. This was introduced by covering part of the bond surface, the prospective crack face, with grease so as to stop the bonding action. All sharp pre-cracks had a length of 25 mm. In all cases the specimens were optically tested using the CGS interferometer for any residual stresses on the bond. Specimens showing signs of residual stresses were discarded.

(i) *Drop-weight tower experiments*

The first series of dynamic tests were performed using a drop-weight loading device to provide impact loading at low to intermediate loading rates. The specimens used had a width of 127 mm, a total length of 305 mm and a thickness of 9 mm. Only specimens containing blunt starter notches were tested in this configuration. The notch length of 25 mm was used so as to provide a crack-to-width ratio (a/W) of 0.2. This ratio has been seen in the past to produce reliable results for homogeneous materials. In Tippur *et al.* (1991) and Lee & Rosakis (1993) it was shown that for a three-point bend edge cracked plate with a/W of 0.2 a significant area of static K-dominance was present around the crack tip. (A region of K-dominance is defined as one in which the stresses are well described by the leading, square-root singular, term of the theoretically predicted asymptotic stress field surrounding the crack tip.)

The drop-weight tower used was a model 8100-A Dynatup tower with a 200 kg free-falling weight. The impactor tup was instrumented so as to provide a time history of the load applied on the specimen. The PMMA–steel or aluminium specimens were supported by resting them on two very thin glass slides, thus approximating a one-point bend test configuration (i.e. negligible reaction forces).

True symmetric one or three-point bend loading can not be achieved dynamically since it is extremely difficult to apply the impact load exactly on the interface, which is about 100 μm thin. In addition, since the wave speeds of PMMA and steel (or aluminium) are vastly different (see table 1) the loading history at the crack-tip would be completely different depending on which side of the bond line impact occurred. Having such an experimental uncertainty was unacceptable. Thus, it was chosen to consistently impact the specimen a small distance (7 mm) into the metal side of the bond. The reason we chose to impact the metal side is that even at moderate impact speeds, PMMA tends to shatter around the impact point.

In all drop-weight experiments the nominal impact velocity used was 4 m s^{-1}. This would correspond to an intermediate loading rate at the crack-tip. (A measure of the loading rate can be provided by the rate of increase of the amplitude of the time-dependent stress intensity factor $K^{d}(t)$. From subsequent analysis of experimental data (§ 3) we can quantify a low loading rate as being less than 10^4 MPa $m^{1/2}$ s^{-1} and a high loading rate as being over 10^6 MPa $m^{1/2}$ s^{-1}.) Intense stress waves generated by impact and reflected from the specimen boundaries, load the notch tip up to crack initiation. The initiated crack-tip then propagates dynamically along the interface. The technique of CGS in transmission was used in conjunction with high-speed photography to record dynamic crack-tip fields in a region approximately 50 mm in diameter around the crack-tip. The light source used was a Spectra-Physics Argon-ion pulsed laser (model 166-09) operating at a wavelength of $\lambda = 514.5$ nm (green light). The beam emerging from the PMMA was processed by two diffraction gratings

located a distance Δ=50 mm apart. The gratings were provided by the Photosciences Co. (Torrance, CA). They are line gratings on glass with a 40 line mm^{-1} ruling. This corresponds to a pitch $p = 0.0254$ mm. The angular sensitivity of the interferometer with these settings is 0.015° per fringe. Both gratings were anti-reflection coated to avoid light-intensity loss and ghost images created by multiple reflections in the inter-grating distance Δ.

After emerging from the second grating, the light is collected by a high-speed camera. Filtering of the -1 diffraction order occurs inside the camera by internal separation of the beams. The camera focuses the (undeformed) specimen surface onto the film track. The high-speed camera is of the rotating mirror type (Cordin Co., model 330A). A rotating mirror attached to a compressed air driven turbine shaft, reflects the image on to a film track which is on a stationary drum surrounding the mirror. The turbine shaft rotates at high speeds (up to 8000 rps) and the image is swept over the film track. Individual frames are obtained by operating the laser light source in a pulsed mode. High-power, short-duration pulses are produced to expose individual frames on the film track. The film exposure time is the duration of each pulse. The interframe time is the time between successive pulses. Because of the high propagation speeds involved in any dynamic crack growth experiment, a very short exposure time is needed to avoid image blurring. The exposure time used in all experiments was 30 ns. A typical interframe time used (i.e. time between pulses) was 1.2 μs (about 840 000 frames s^{-1}).

When the camera operates at the above mentioned framing rate, the total image recording time is about 95 μs. This is because the total number of frames obtainable by this camera is 80. The time of 95 μs is a very short window of observation. Therefore, precise triggering of the laser is very important. A strain gauge placed on the specimen at the point of impact senses the impacting tup. Its output is then delayed appropriately and the resulting signal is used to trigger the light source.

A typical sequence of selected interferograms from a drop-weight tower test is shown in figure 5 (from Tippur & Rosakis 1991). These are from a PMMA–aluminium configuration impacted at 2 m s^{-1}. Frames at 14 μs intervals are shown.

(ii) *Gas gun experiments*

In an attempt to initiate crack propagation along the interface under different mixity conditions (i.e. different ratios of opening to shearing crack-face displacement) to those obtainable in the drop-weight tower, it was decided to impact the bimaterial specimens using a high-speed gas gun. Such a gun can produce higher loading rates than a drop-weight device, even though it usually sustains the loading for a shorter time. Even so, it is possible with a high enough loading rate to initiate the crack in a very short time period. The gas gun used in our experiments was manufactured in-house. It is capable of firing a 75 mm long, 50 mm diameter, steel projectile at speeds up to 100 m s^{-1}. However, in all experiments presented in this work, the impact velocity was 20 m s^{-1}. The same optical technique and recording system as for the drop-weight tower experiments were used.

The loading geometry used was that of one-point bend. A series of such tests was performed, during all of which the steel side was the one impacted, exactly as was the case in all drop-weight experiments. Each specimen was tested while having either a starter notch (750 μm wide) or a sharp starter crack. A typical sequence of interferograms resulting from a one-point bend air-gun test (sharp starter crack used) is shown in figure 6. Again, only the PMMA side of the specimen produces

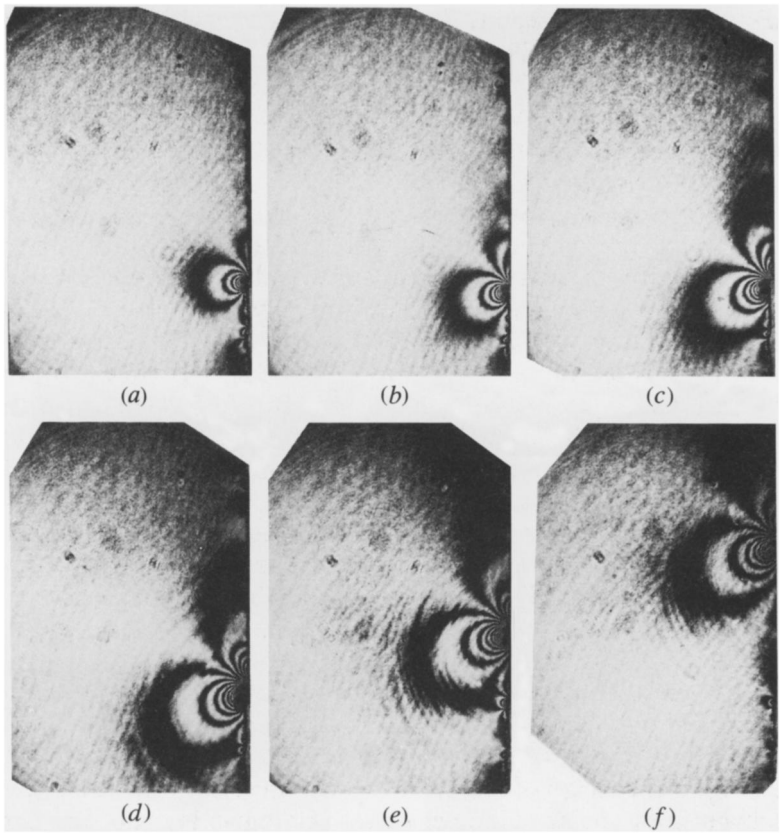

Figure 5. Selected sequence of CGS interferograms from a PMMA–aluminium three-point bend drop-weight tower test. (*a*) $t = -42$ μs; (*b*) $t = -28$ μs; (*c*) $t = -14$ μs; (*d*) $t = 0$ μs; (*e*) $t = 14$ μs; (*f*) $t = 28$ μs. (From Tippur & Rosakis 1991.)

fringes since it is transparent. A detailed qualitative and quantitative analysis of the fringe patterns will be made in the next section.

3. Subsonic crack growth along bimaterial interfaces

(*a*) *Experimental observations*

(i) *Drop-weight tower experiments*

Several experiments were performed using the drop-weight tower device. A sequence of interferograms from a PMMA–aluminium three-point bend test is shown in figure 5. Time $t = 0$ μs corresponds to the time of crack initiation. Interferograms at negative times have been taken before initiation. In general terms, the size of the fringe pattern surrounding the tip depends mainly on the magnitude of the stress field around it. In addition, the particular orientation of each lobe of the pattern is dependent on the relative amounts of normal (opening) to shearing stresses around the tip (i.e. the stress mixity). It is clearly visible in figure 5 that at times before initiation, the size and rotation of the fringe pattern changes as time progresses. This represents changing conditions of the stress field around the original notch tip due

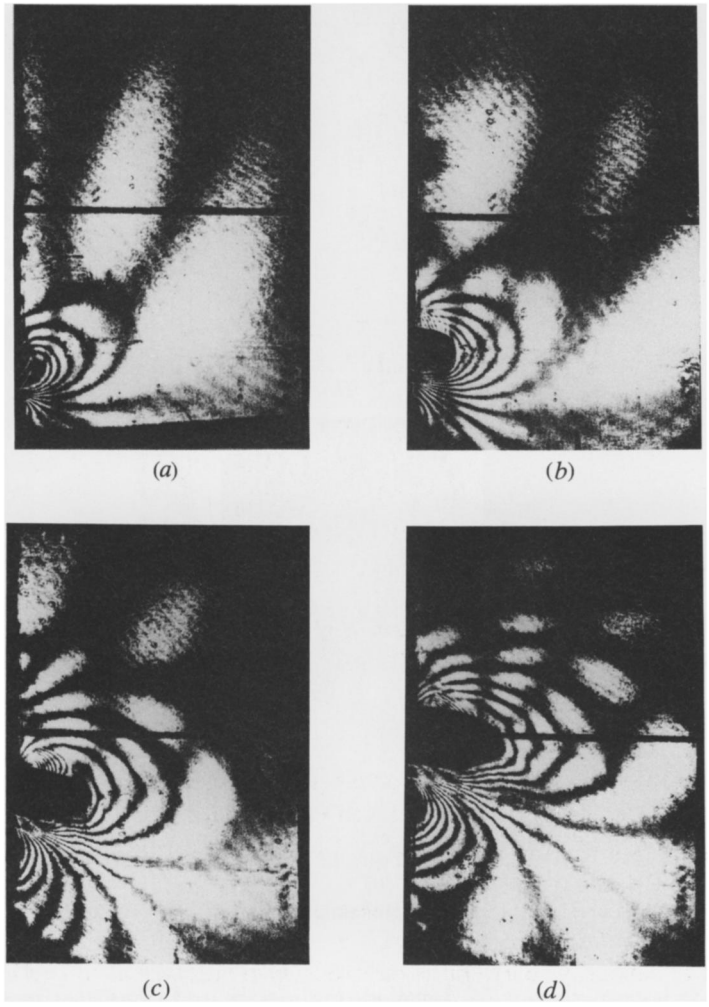

Figure 6. Selected sequence of CGS interferograms obtained from a one-point bend air-gun test on a PMMA–steel specimen. (*a*) $t = 3$ μs; (*b*) $t = 8$ μs; (*c*) $t = 13$ μs; (*d*) $t = 16.5$ μs.

to the arrival of stress waves from the impact area and the specimen boundaries. At some time instant, close to $t = 0$ μs, conditions are favorable for notch initiation.

Up to the time of notch initiation we can provide a fairly clear qualitative description of the loading history of the initial notch tip, simply by looking at stress wave propagation in the specimen. After the specimen is impacted, on the metal side, a compressive stress pulse travels its vertical width (figure 7*a*). It is reflected as a tension pulse from the traction free end on the bottom of the plate (figure 7*b*) and shortly thereafter reaches the still stationary notch tip, providing primarily shear loading. Indeed, at this point in time ($t = -42$ μs), the fringe pattern seems primarily shear dominated. However, the magnitude of the stresses is not sufficient to initiate a running crack. Although impact is always on the side of the metal, a part of the initial impact pulse will also be transmitted into the PMMA side because of the existence of the bond. However, waves in the metal side travel much faster than in the PMMA side, so not only does the wave generated upon impact reach the notch

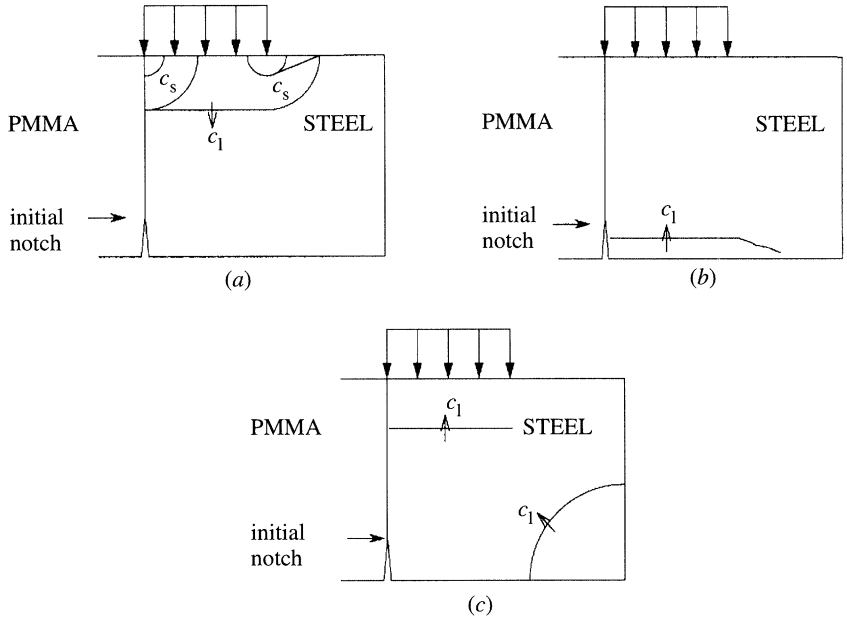

Figure 7. Schematic describing the predominant interactions of stress waves with the interfacial crack-tip for the drop-weight tower experiments (*a*) just after the impact; (*b*) just after reflection of initial pulse; (*c*) just before crack initiation.

tip from the metal side first, but also subsequent reflections in the metal side arrive first at the notch tip. Essentially, what has happened in the times corresponding to figure 7*b* is that the steel side has moved vertically with respect to the PMMA, which has not been displaced yet.

A time of about 65–70 μs passes between the time of impact and the time of crack initiation. In this time no waves traveling in the PMMA have reached the notch tip. The time of initiation correlates very well with the arrival of the first unloading wave generated at the lower corner of the metal side of the bond (figure 7*c*). This wave is a tensile release wave that impinges on the notch at almost 80°. It therefore induces a near-tip field that contains a substantial opening component. This causes the observed fringe pattern to rotate into what is a primarily opening-dominated mode. The stress field achieves appropriate conditions for notch initiation (e.g. such as the attainment of a critical pair of G and ϕ as described in figure 1), and a crack starts propagating dynamically along the interface. It is clear that, because of the very short time between specimen impact and crack initiation, all deformation effects visible in the interferograms of the PMMA side are from leakage of energy from the metal side to the PMMA through waves crossing the interface. Essentially throughout all tests, the crack is driven by the metal side of the bond.

In contrast to the pre-initiation stages, the fringe pattern around the propagating crack-tip does not change much either in size or orientation (see figure 5). Indeed, this was a phenomenon that was consistently observed in all experiments performed in this study. This suggests that the stress and deformation fields surrounding the crack-tip remain relatively constant throughout crack propagation. It is the recognition of this fact that provided the strong suspicion that some fundamental physical quantities, such as stresses or crack-face displacements, must remain constant during

crack propagation. In § 4, where a particular fracture criterion will be proposed, we will investigate this further.

Typical crack-tip speed and acceleration histories corresponding to a PMMA–steel experiment are shown in figures 8*a* and *b*. Note that values of acceleration are only meant to be illustrative, because of the errors involved in two successive differentiations. The crack-tip speed increases to the largest value it attains within our window of observation in a very short time (about 15 μs). This is evident by the presence of large crack-tip accelerations at the beginning of crack growth. Consistent with the observation of stress waves emanated from the tip during crack growth (visible in figure 5) is the measured maximum crack-tip speed. This is seen to be around $800\ \mathrm{m\,s^{-1}}$ or $0.85c_{\mathrm{R}}^{\mathrm{PMMA}}$. This observation was rather surprising given previous experience with dynamic crack growth in homogeneous PMMA specimens of the same configuration and loading (maximum speeds of $\sim 0.6c_{\mathrm{R}}^{\mathrm{PMMA}}$).

(ii) *Gas gun experiments*

A sequence of selected interferograms from a gas gun test is shown in figure 6. The resulting crack-tip speed and acceleration histories for this particular test are shown in figures 9*a* and *b*. It is clear that in this case the crack-tip speed has exceeded both the Rayleigh ($c_{\mathrm{R}}^{\mathrm{PMMA}}$) and the shear ($c_{\mathrm{s}}^{\mathrm{PMMA}}$) wave speed of PMMA and is rapidly approaching $1.5c_{\mathrm{s}}^{\mathrm{PMMA}}$ (recall $c_{\mathrm{R}}^{\mathrm{PMMA}} = 920\ \mathrm{m\,s^{-1}}$ in plane stress and $c_{\mathrm{s}}^{\mathrm{PMMA}} = 1000\ \mathrm{m\,s^{-1}}$). Observations and results for crack growth exceeding $c_{\mathrm{s}}^{\mathrm{PMMA}}$ will not be discussed in this paper. The details on this aspect of the experiments may be found in Lambros & Rosakis (1995). In the current work we will only focus on the case of subsonic crack growth, and in particular on $\nu < c_{\mathrm{R}}^{\mathrm{PMMA}}$ (ν = crack-tip speed).

It is possible to apply similar wave propagation arguments, as in the previous section, to provide a physical explanation of the fracture process in the case of the high-speed gas gun tests. In the gas gun experiments it was observed that the time of crack initiation was around 30 μs after impact. In this case therefore the influence of the metal side on crack propagation is even more pronounced than before, since in 30 μs a dilatational wave in PMMA travels less than half the specimen width. In the gas gun tests, crack initiation occured earlier because of the higher impact velocities used. In all air gun tests, the steel side of the specimen was impacted at $20\ \mathrm{m\,s^{-1}}$. This is five times larger than the impact velocity used in the drop-weight tests. This means that the initial compressive wave generated by the air gun is approximately five times more intense than that generated by the drop-weight tower.

Figure 7 shows a sketch of the wave propagation occurring in the metal side of the specimen at short times after impact in the drop-weight experiments. The situation in the air gun experiments is very similar. The main dilatational wave generated at impact is almost normal to the interface and is traveling parallel to it. Thus it loads the crack-tip in a shear fashion. The wave then reflects off the bottom surface as a tension wave and reloads the crack-tip again in shear. At times corresponding to the situations shown in both figure 7*a* and *b*, the stress state surrounding the initial crack-tip is shear dominated; exactly as it was shear dominated in the drop-weight tower tests at similar times after impact. The difference in this case is that the compressive wave is strong enough to cause crack initiation at very short times, when the crack-tip stress fields are still shear dominated. Indeed, the observed initiation time of about 30 μs correlates well with the time it takes a dilatational wave to travel the width of the specimen, reflect off the bottom surface of the metal side and reach the tip once again. When analysing the results we therefore expect to see a

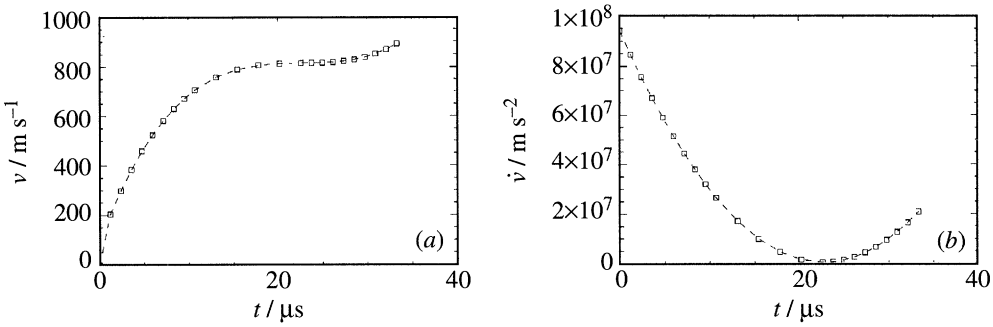

Figure 8. Typical (*a*) velocity and (*b*) acceleration time histories for PMMA–steel drop-weight tower experiment.

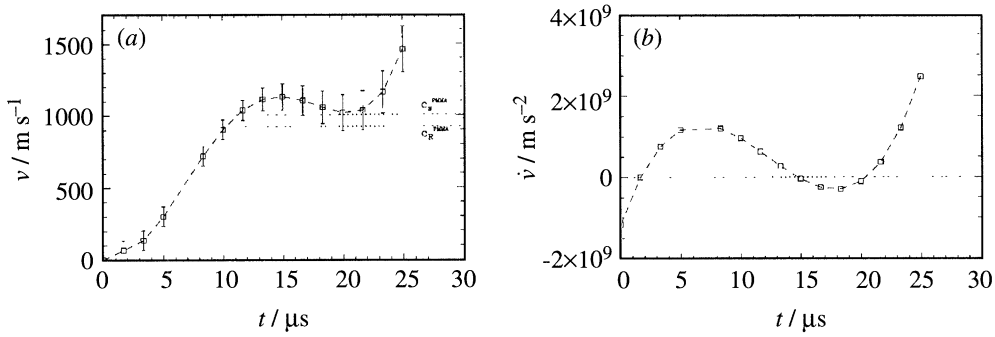

Figure 9. (*a*) Velocity and (*b*) acceleration time histories for the experiment shown in figure 6.

significant difference in the stress mixities at initiation (and probably propagation) between the drop-weight tower and air gun tests. The former are expected to be more opening-mode dominated and the latter more shear-mode dominated. Quantitative evidence that growth in the gas gun experiments is more shear dominated than in the drop-weight experiments is provided in § 4.

(*b*) *Theoretically predicted crack-tip fields and data reduction*

The asymptotic nature of the stress field surrounding interfacial cracks propagating dynamically in bimaterial systems was initially studied by Yang *et al.* (1991). Their analysis assumed steady-state conditions and provided the spatial structure of the square-root singular stress field at the vicinity of the crack tip. This field was then used to define the notion of a dynamic complex stress intensity factor K^{d}. Motivated by the present experimental observations of high transient effects (e.g. high crack-tip accelerations as seen in figures 8 and 9), Liu *et al.* (1993) relaxed the steady-state assumption and performed a higher order, fully transient asymptotic analysis. Their results revealed that the leading term of their transient asymptotic expansion had an identical spatial structure as the one obtained by Yang *et al.* (1991). However, the crack-tip speed and complex-stress intensity factor were allowed to assume their instantaneous values. The higher order contributions were found to depend strongly on crack-tip acceleration and rate of change, $\dot{K}^{\mathrm{d}}(t)$, of the dynamic complex stress intensity factor.

The x_1-gradient of $\hat{\sigma}_{11} + \hat{\sigma}_{22}$ for material 1 (above the interface), as obtained by considering only the leading term of the transient asymptotic expansion for stress

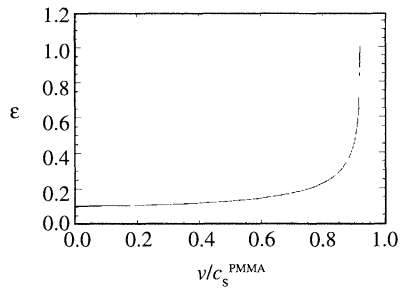

Figure 10. Variation of oscillatory index with velocity for a PMMA–steel bimaterial system (plane stress conditions).

by Liu *et al.* (1993) is given by

$$
\begin{aligned}
&c_\sigma h \frac{\partial(\hat{\sigma}_{11}+\hat{\sigma}_{22})}{\partial x_1} \\
&\quad = \frac{c_\sigma h r_1^{-3/2} \mathrm{e}^{-\varepsilon(\pi-\theta_1)} A}{2\sqrt{2\pi}} \Big[-(1+\alpha_s^2-2\eta\alpha_s)\mathrm{e}^{2\varepsilon(\pi-\theta_1)} \cos(\tfrac{3}{2}\theta_1-\phi-\varepsilon\ln r_1) \\
&\quad -(1+\alpha_s^2+2\eta\alpha_s)\cos(\tfrac{3}{2}\theta_1+\phi+\varepsilon\ln r_1) \\
&\quad +2\varepsilon(1+\alpha_s^2-2\eta\alpha_s)\mathrm{e}^{2\varepsilon(\pi-\theta_1)}\sin(\tfrac{3}{2}\theta_1-\phi-\varepsilon\ln r_1) \\
&\quad -2\varepsilon(1+\alpha_s^2+2\eta\alpha_s)\sin(\tfrac{3}{2}\theta_1+\phi+\varepsilon\ln r_1)\Big], \qquad (5)
\end{aligned}
$$

where

$$
A = \frac{(\alpha_1^2-\alpha_s^2)|K^d(t)|}{(4\alpha_1\alpha_s-(1+\alpha_s^2)^2)\cosh(\varepsilon\pi)}, \qquad \alpha_{1,s} = \left(1-\frac{v^2}{c_{1,s}^2}\right)^{1/2},
$$

$$
\theta_1 = \arctan[(\alpha_1 x_2)x_1], \quad r_1 = \sqrt{x_1^2+\alpha_1^2 x_2^2},
$$

$$
K^{\mathrm{d}}(t) = K_1^{\mathrm{d}}(t) + \mathrm{i}K_2^{\mathrm{d}}(t), \quad \phi(t) = \arctan(K_2^{\mathrm{d}}(t)/K_1^{\mathrm{d}}(t)),
$$

x_1, x_2 are Cartesian coordinates of a coordinate system translating with the crack-tip at speed $v(t)$, $K^{\mathrm{d}}(t)$ is the instantaneous value of the complex dynamic stress intensity factor, $c_{1,s}$ are the longitudinal and shear wave speeds respectively and $\varepsilon = \hat{\varepsilon}(v)$, $\eta = \hat{\eta}(v)$ are functions of crack-tip speed and material properties. Parameters ε and η are two mismatch parameters that characterize the interface. They are derived in Yang *et al.* (1991) and discussed further in Liu *et al.* (1993). ε is called the (dynamic) oscillatory index and η the traction resolution factor.

The variation of ε with crack-tip speed is shown in figure 10. This figure is for a PMMA–steel bimaterial combination having the material properties shown in table 1. The plot is for crack-tip speeds below the Rayleigh wave speed of PMMA, which is the regime in which equation (5) is valid. The parameters are such that $\varepsilon \to \varepsilon_s$, $\eta \to 1$ as $v \to 0$ and (5) reduces to the quasi-static expression for stress gradients. ε_s is the well known quasi-static oscillatory index. It can clearly be seen in figure 10 that ε is an increasing function of crack-tip speed, but for low values it does not vary drastically. At around 60–70% of the shear wave speed of PMMA it increases rapidly and becomes unbounded as the crack-tip speed approaches the Rayleigh wave speed

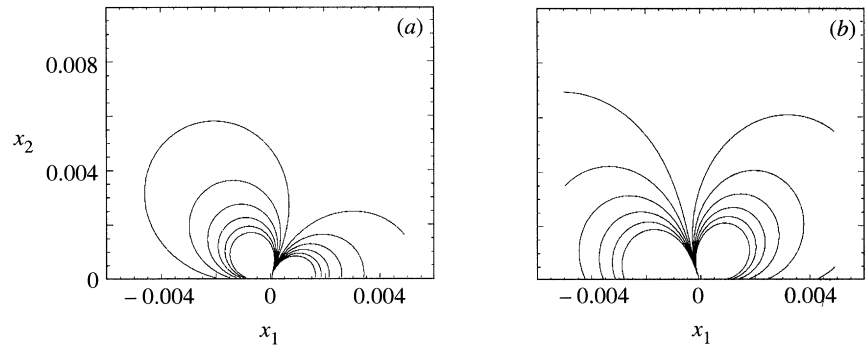

Figure 11. Theoretically predicted fringe patterns, from (5), at two different values of crack-tip speed ($|K^{\mathrm{d}}| = 1\ \mathrm{Pa\ m^{1/2}}$, $\phi = 45°$); $v/c_{\mathrm{s}}^{\mathrm{PMMA}}$ = (*a*) 0.3, (*b*) 0.8.

of PMMA (dotted line in figure 10). This implies that elastic property mismatch effects will become more dominant as the crack-tip speed increases.

It is possible to investigate the influence of dynamic effects (inertia) on simulated CGS fringe patterns by plotting contours of (5) for different values of crack-propagation velocity. Such plots are shown in figures 11*a* and *b*. Values of $|K^{\mathrm{d}}| = 1\ \mathrm{Pa\ m^{1/2}}$ and $\phi = 45°$ have been used in both figures 11*a* and *b*. The difference between the two is that they represent crack growth at speeds $v = 0.3c_{\mathrm{s}}^{\mathrm{PMMA}}$ and $v = 0.8c_{\mathrm{s}}^{\mathrm{PMMA}}$ respectively. Clearly, the orientation of the stress field depends considerably on crack-tip speed. This effect is created by the presence of the term $\varepsilon \ln r_1$ in the arguments of the sines and cosines in (5). It is a complementary effect to a change in phase angle ϕ.

In (5) only the time-dependent values of the dynamic complex stress intensity factor and crack-tip speed are undetermined by the asymptotic analysis. In each experiment, the values of $K^{\mathrm{d}}(t)$ will depend on the particular geometry and loading and have to be determined experimentally. They are also expected to vary with time as reflected waves from the specimen boundaries return to the crack-tip. We can use (5) to extract K^{d} as a function of time from optical interferograms like those seen in figures 5 and 6. Extraction of parameters like K^{d} is possible provided that experimental data are gathered from a region near the moving crack-tip characterized by the structure presented in (5), i.e. that there is a finite region of K^{d}-dominance outside the region of three-dimensional deformation that will invariably exist around the crack tip (see figure 3). (For a discussion on the influence of higher order terms see Liu *et al.* (1993).)

(*c*) *Results of experimental data*

The main goal of this research project is to identify a physically meaningful and accurate criterion governing dynamic crack propagation along bimaterial interfaces. Traditionally, for historical reasons and engineering applicability, dynamic fracture criteria in homogeneous materials have been formulated in terms of the homogeneous stress-intensity factor $K_{\mathrm{I}}^{\mathrm{d}}$ (Kanninen & Popelar 1985; Freund 1990). Also, quasi-static initiation criteria for bimaterial cracks have been based on the energy release rate G and phase angle ϕ of a K-dominant field, as explained in § 1. No criterion has ever been proposed for dynamic crack growth in bimaterials. To be able to compare with existing criteria in special cases we shall also attempt to formulate a dynamic propagation criterion using the notion of a dynamic complex stress intensity factor

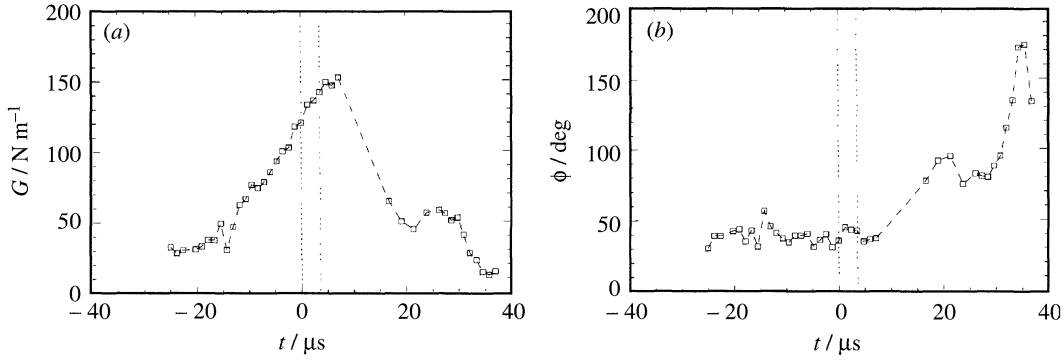

Figure 12. Time history for energy release rate and phase angle ($L = 1$ m) for a typical PMMA–steel drop-weight tower experiment.

K^{d} (or alternatively G^{d} and ϕ). All results presented in this section, and used in § 4 to determine a fracture criterion, are from interferograms in which a K^{d}-dominant region could be established.

Time histories of the energy release rate G^{d} and phase angle ϕ for a PMMA–steel drop-weight tower test are shown in figures 12*a* and *b*. For the case of dynamic interfacial crack growth, G^{d} is related to $|K^{\mathrm{d}}|$ by (Yang *et al.* 1991)

$$G = F(v)\left|K^{\mathrm{d}}\right|^2/4\mu_1, \tag{6}$$

where F is a known function of velocity and mechanical properties of the interface constituents, explicitly given in Yang *et al.* (1991) and μ_1 is the shear modulus of material 1. Note that, unlike crack growth in homogeneous solids, F is finite at the Rayleigh wave speed of PMMA. The phase angle in figure 12*b* has been calculated from:

$$\phi = \arctan\left(K_2^{\mathrm{d}}/K_1^{\mathrm{d}}\right). \tag{7}$$

This implies that a length scale of $L = 1$ m has been used in this particular plot. The phase angle ranges from $-\pi$ to π to cover all possible sign combinations of K_1^{d} and K_2^{d}.

In figure 12, $t = 0$ μs corresponds to the estimated time of crack initiation. Pre-initiation values of G^{d} and ϕ were determined by fitting the quasi-static stress field to interferograms before $t = 0$ μs. The uncertainty in time of initiation is represented in figure 12 by the two dotted vertical lines.

The energy release-rate G^{d} increases to a peak a little after $t = 0$ μs and then drops to a value close to zero, implying that the process of dynamic crack propagation along interfaces is highly unstable, at least in the particular experimental configurations and loading rates used in this study. This result is corroborated by the steep rise of the crack-tip speed in very short times. On the other hand, the phase angle ϕ increases throughout the test. The change in phase angle can be expected simply by looking at the dynamic interferograms. It was pointed out in § 3 *a* (i) that the CGS fringe pattern surrounding the propagating crack-tip does not change much with time either in size or orientation. This was clearly illustrated in figure 5. However, in figures 11*a* and *b* it was seen that the theoretically predicted fringe pattern from a K^{d}-dominant field rotates if the crack-tip speed v changes, but $|K^{\mathrm{d}}|$ and ϕ remain fixed. Both the phase angle ϕ and velocity v affect the orientation of the stress field as seen in the argument of the sines and cosines in (5). We have seen experimentally

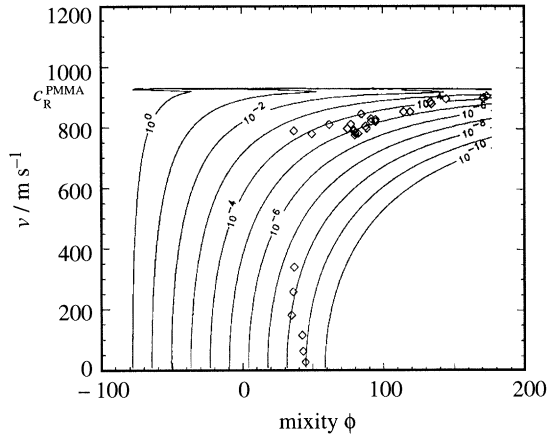

Figure 13. Magnitude of predicted contact zone in PMMA–steel one-point bend drop-weight tower experiments.

that v changes drastically with time. Thus the phase angle ϕ has to vary in such a way so as to keep the fringe pattern the same throughout propagation. In effect, the variation of ϕ cancels the influence that the changing v has on the fringe pattern.

The link between the variations of v and ϕ will be used in the next section to propose a dynamic crack-growth criterion.

Because of the presence of oscillatory terms in the stress field shown in (5), all pathologies associated with the theory of static linear elastic interfacial mechanics are still present. Of paramount importance is the pathology of predicted interpenetration of the crack faces. The extent of the resulting contact zone is given by (Rice 1988)

$$r_c = \exp([-\tfrac{1}{2}\pi - \phi + \arctan(2\varepsilon)]/\varepsilon). \tag{8}$$

This is the same as for the static case, but with ϕ and ε changing with velocity. To accept the measured values of G^d and ϕ as accurate we must make sure that the extent of predicted contact is much smaller than the smallest characteristic length of the experimental configuration. From figure 10 it can be seen that as $v \to c_R^{PMMA}$, $\varepsilon \to +\infty$. As v, and consequently ε, gets larger it would seem that the predicted contact zone r_c would become unacceptably large. However, when calculating r_c from experimental measurements, it was found that the variation of ϕ suppressed the increase of the contact-zone size, keeping it at very low values for all but the highest crack-tip velocities. An idea of the size of the contact zone predicted for a one-point bend PMMA–steel test is given in figure 13. The solid lines are contours of constant contact zone size, as derived from (8) for a range of v and ϕ. The diamond points are the calculated results from three nominally identical PMMA–steel one-point bend drop-weight tower tests. Clearly values of the contact zone are below 10^{-4} m. This is well within the zone of three-dimensional deformation surrounding the crack tip whose minimum extent is around 2 mm.

Very similar results are obtained when analysing the interferograms shown in figure 5. The variations of G^d and ϕ with time for the propagation part of this experiment are shown in figures 14*a* and *b*. The general trends are similar to those corresponding to the other drop-weight tower experiments reported above. However, the values measured are drastically different to the values initially quoted by Tippur

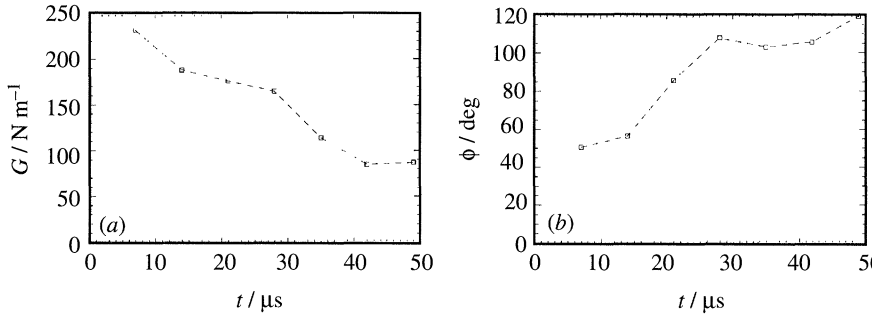

Figure 14. Time history of energy release rate and phase angle ($L = 1$ m) for the experiment shown in figure 5.

& Rosakis (1991), obtained on the basis of a quasi-static analysis of the experimentally captured fringe patterns.

Results from air gun experiments are qualitatively similar. However, the values of G^{d} and ϕ obtained in these experiments correspond to a shear-dominated process (see § 4).

4. A criterion for dynamic interfacial crack growth

(a) *Proposed fracture criterion based on crack face profile*

As was pointed out in § 3 a (i), in regards to figure 5, before crack initiation ($t < 0$ μs) the fringe pattern around the tip changes both in size and orientation, denoting a change in the stress field surrounding the crack. In contrast, after initiation, the fringe pattern surrounding the propagating crack does not change significantly with time. The implication of this visual observation is that some fundamental physical quantity, such as stress or crack-face displacement, must remain constant throughout the crack growth phase. It has already been established that v, ϕ and G^{d} (or $|K^{\mathrm{d}}|$) all vary considerably during crack growth. Therefore, if we wish to mathematically model the fact that the fringe pattern during crack growth does not change, we must employ some combination of these three quantities that remains constant.

We begin the search for a growth criterion by referring to the discussion of § 3 c where it was observed that the lack of rotation of the fringe pattern surrounding the propagating crack must be linked to the simultaneous variation of v and ϕ. Indeed, this variation must be such as to eliminate any net rotation of the fringe pattern. Recall that (5) contains trigonometric functions (responsible for the amount of fringe rotation) whose arguments involve ϕ and $\varepsilon(v) \ln r_1$. To investigate the relationship between v and ϕ experimental results have been plotted in the (ϕ, v)-plane in figure 15. The experimental results are shown as diamonds and squares. The diamonds correspond to the results of three nominally identical PMMA–steel one-point bend experiments conducted under drop-weight tower impact. The squares correspond to the results of three nominally identical PMMA–steel one-point bend experiments conducted under gas gun projectile impact. It can be seen in both cases that as the crack-tip speed approaches $c_{\mathrm{R}}^{\mathrm{PMMA}}$ the phase angle ϕ increases. As expected from our previous discussion, initiation of crack growth happens at different mixities (i.e. different ϕ at $v = 0$ m s^{-1}) indicating that the gas gun experiments are more shear dominated than their drop-weight tower counterparts.

We first seek a near-tip quantity, involving v and ϕ only, which will remain constant

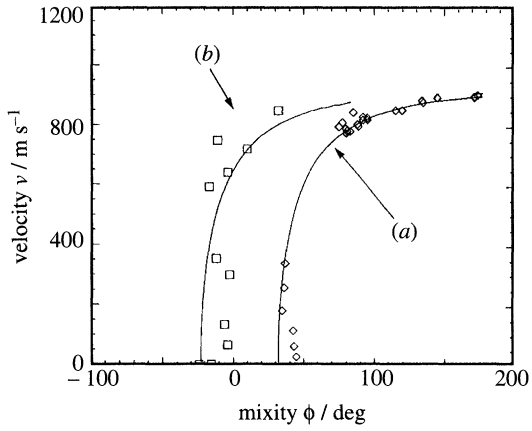

Figure 15. Fit of (12) (a = 2 mm) to experimental data from typical one-point bend (a) PMMA–steel drop-weight tower (v_i = 4 m s^{-1}, δ_1/δ_2 = −0.3) and (b) gas gun impact (v_i = 20 m s^{-1}, δ_1/δ_2 = −3) tests.

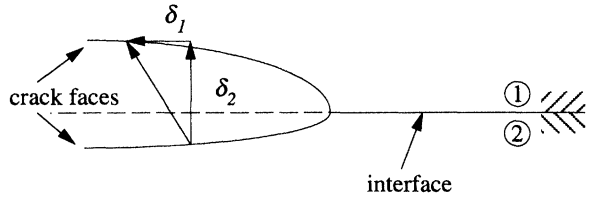

Figure 16. Schematic definition of opening and shearing diplacements behind interfacial crack tip.

throughout crack growth in each set of experiments. A candidate for such a quantity is the ratio of the opening (δ_2) to shearing (δ_1) displacements behind the crack tip. They are defined as

$$\delta_\alpha(r) = u_\alpha(r, \theta = +\pi) - u_\alpha(r, \theta = -\pi), \quad \alpha = 1, 2, \tag{9}$$

where $u_\alpha(r, \theta)$ is the displacement field surrounding the crack tip. Figure 16 shows a geometrical representation of δ_1 and δ_2 behind the crack-tip. A positive δ_2 represents an opening displacement, while a positive δ_1 represents sliding of material 1 along the positive x_1-axis.

To quantify the relative amounts of opening to shearing displacements we can define a displacement mixity as follows:

$$\gamma = \arctan\left(\delta_1/\delta_2|_{r=a}\right). \tag{10}$$

A value of $\gamma = 0°$ denotes pure opening whereas a value of $\gamma = \pm 90°$ denotes pure shearing of the crack faces.

From the asymptotic analysis of Yang *et al.* (1991), the crack-face displacements are given by,

$$\left.\begin{aligned} \delta_1(r) &= \frac{H_{22}}{\cosh(\pi\varepsilon)}\sqrt{\frac{2r}{\pi}}\frac{|K^{\mathrm{d}}|}{\sqrt{1+4\varepsilon^2}}\frac{1}{\eta}\sin\left(\phi + \varepsilon\ln r - \arctan(2\varepsilon)\right), \\ \delta_2(r) &= \frac{H_{22}}{\cosh(\pi\varepsilon)}\sqrt{\frac{2r}{\pi}}\frac{|K^{\mathrm{d}}|}{\sqrt{1+4\varepsilon^2}}\cos\left(\phi + \varepsilon\ln r - \arctan(2\varepsilon)\right). \end{aligned}\right\} \tag{11}$$

Quantities ε and η have been previously defined and the function H_{22} is given in Yang *et al.* (1991). Each of the two displacements in (11) depends on $|K^{\mathrm{d}}|$, but their ratio is only a function of v and ϕ. If we assume that throughout propagation the ratio δ_1/δ_2 remains constant, say at a value c_1, at a fixed distance, say a, behind the crack-tip, then we can write

$$\left.\frac{\delta_1}{\delta_2}\right|_{r=a} = C_1 = \frac{1}{\eta}\tan\left(\phi + \varepsilon \ln a - \arctan\left(2\varepsilon\right)\right),$$

or, solving for ϕ,

$$\phi = \phi\left(v\right) = \arctan\left\{\eta\left(v\right) C_1\right\} + \arctan\left\{2\varepsilon\left(v\right)\right\} - \varepsilon\left(v\right)\ln a. \tag{12}$$

Equation (12) defines a single line in the (v, ϕ)-plane (for a given c_1 and a). The dependence of ϕ on v comes in through the velocity dependence of the oscillatory index ε (see figure 10) and the traction resolution factor η.

The analytical relation between ϕ and v resulting from the assumption $\delta_1/\delta_2|_{r=a} = C_1$ is displayed twice in figure 15, along with the experimental results, for two different values of the constant c_1 (solid lines). These two lines are obtained for $a = 2$ mm and $c_1 = -0.3, -3$. Each line follows a set of experimental data points corresponding to each of the loading cases examined. From the agreement of the analytical curves with the data, we conclude that for each class of experiments δ_1/δ_2 remains constant throughout crack propagation. For the case of the drop-weight tower experiments (impact speed $v_i = 4\ \mathrm{m\,s^{-1}}$), $c_1 = -0.3$. This implies that the amount of crack face opening is 3.3 times the amount of crack face sliding, thus indicating growth at a primarily opening mode at this particular distance behind the tip. At this location the displacement mixity (defined in (10)) is about $\gamma = -17°$. For the case of the gas gun experiments (impact speed $v_i = 20\ \mathrm{m\,s^{-1}}$), $c_1 = -3$. Consequently, the magnitude of the shearing displacement is now 3 times greater than the magnitude of the opening displacement behind the crack tip (once again at a distance of 2 mm). This observation verifies our earlier expectations that the gas gun experiments are 'shear'-dominated (recall wave propagation arguments presented in § 3 *a* (ii)). In this case, the displacement mixity at the same location of 2 mm is $\gamma = -72°$.

The condition of a constant δ_1/δ_2 behind the crack tip in (12) cannot constitute a dynamic crack growth criterion on its own because it does not predict the magnitude of the stresses surrounding the propagating crack. It may form part of a propagation criterion that relates the phase angle with the crack-tip speed. However, the size of the stress field, and the CGS fringe pattern, surrounding the crack tip is primarily dependent upon $|K^{\mathrm{d}}|$, the magnitude of the complex stress intensity factor. The second part of a fracture criterion would thus have to involve a link between $|K^{\mathrm{d}}|$, v and ϕ.

Assume that in addition to the experimentally observed fact of constant ratio between δ_1 and δ_2 at a distance a behind the crack tip, we also have a constant crack opening displacement, say of value c_2, at the same distance. From (11*b*) this can be expressed as

$$\delta_2\left(a\right) = \frac{H_{22}}{\cosh\left(\pi\varepsilon\right)}\sqrt{\frac{2a}{\pi}}\,\frac{\left|K^{\mathrm{d}}\right|}{\sqrt{1+4\varepsilon^2}}\cos\left(\phi + \varepsilon\ln a - \arctan\left(2\varepsilon\right)\right) = C_2$$

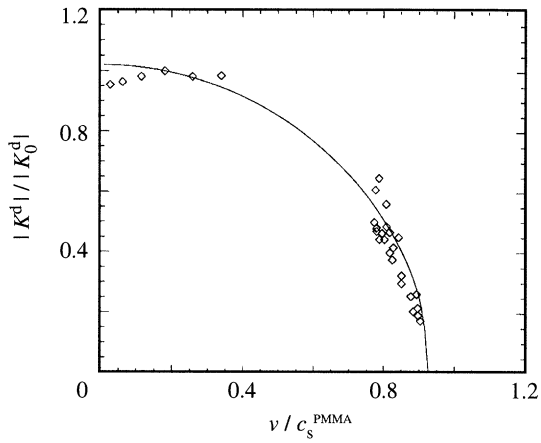

Figure 17. Comparison of normalized stress intensity factor from a PMMA–steel drop-weight tower experiment with the prediction of constant crack profile growth.

or, solving for $|K^{\mathrm{d}}|$,

$$\left|K^{\mathrm{d}}\right| = C_2 \frac{\sqrt{1+4\varepsilon^2}\cosh(\pi\varepsilon)}{H_{22}} \sqrt{\frac{\pi}{2a}} \frac{1}{\cos(\phi + \varepsilon \ln a - \arctan(2\varepsilon))}. \tag{13}$$

The above is a relation between $|K^{\mathrm{d}}|$, v and ϕ with c_2 and a as parameters. For specific values of c_2 and a, (13) represents a surface in the $|K^{\mathrm{d}}|$, v and ϕ space.

By combining the two requirements (i.e. substituting (12) into (13)), we obtain a relation between $|K^{\mathrm{d}}|$ and v only. This relation is therefore obtained by simultaneously requiring that δ_1/δ_2 is constant at some distance behind the crack tip, as has already been observed experimentally, and in addition that δ_2 is constant at the same location. The combination of (12) and (13) yields

$$\left|K^{\mathrm{d}}\right| = C_2 \frac{\sqrt{1+4\varepsilon^2}\cosh(\pi\varepsilon)}{H_{22}} \sqrt{\frac{\pi}{2a}} \frac{1}{\cos(\arctan(C_1\eta))}. \tag{14}$$

Equation (14) depends on constants c_1 and c_2. It should be noted that the constant c_1 indirectly depends on our choice of a in a way such that the two parameters provide the best fit to the experimental data in the manner seen in figure 15. In addition, the constant c_2 is related to the (unknown) opening strength of the bond. It is not necessary to *a priori* know this constant since it can be eliminated by normalizing (14) with some reference value. If we assume that one of the experimentally obtained data points, with parameters v_0, ε_0, η_0, H_{22}^0, $|K_0^{\mathrm{d}}|$ and G_0, follows (14), then we can eliminate c_2 by computing $|K^{\mathrm{d}}|/|K_0^{\mathrm{d}}|$ as

$$\frac{\left|K^{\mathrm{d}}\right|}{\left|K_0^{\mathrm{d}}\right|} = \frac{\sqrt{(1+4\varepsilon^2)}\cosh(\pi\varepsilon)\, H_{22}^0 \cos(\arctan(C_1\eta_0))}{\sqrt{(1+4\varepsilon_0^2)}\cosh(\pi\varepsilon_0)\, H_{22} \cos(\arctan(C_1\eta))} = \mathcal{F}(v). \tag{15}$$

Comparison with all other experimental points is now possible by plotting (15) in the $|K^{\mathrm{d}}|$, v plane.

A comparison of the experimental data with (15) for the PMMA–steel drop-weight tower tests used previously is shown in figure 17. The normalizing point used is the one corresponding to $v_0 = 180\ \mathrm{m\ s^{-1}}$. This point is forced to agree with the computed curve (solid line in figure 17), since it has been used to eliminate the constant c_2.

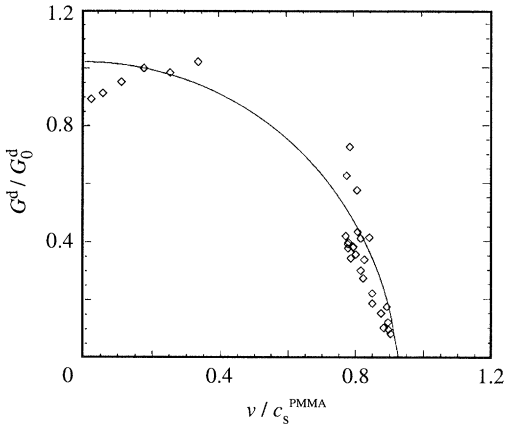

Figure 18. Comparison of normalized energy release rate from a PMMA–steel drop-weight tower experiment with the prediction of constant crack profile growth.

Nevertheless, the remaining points are not forced to follow the curve. It can be seen, however, that agreement is very good. A notable issue here is that the line in figure 17 is not a fit to the experimental values. Only c_1 is fitted to the experimental values using (12) as described above. Once this is done the curve given by (15) is completely specified. The agreement of (15) with experimental data over a wide range of velocities proves that indeed not only is the ratio δ_1/δ_2 constant behind the crack tip, but δ_2 itself is also constant. This observation implies that the crack face profile remains invariant at all time instants during propagation (i.e. $\delta_1(t) = \text{const.}$, $\delta_2(t) = \text{const.}$)

It is possible to convert equations (13), (14) and (15) to display the energy release rate G^d instead of the magnitude of the stress intensity factor $|K^d|$. The quantities G^d and $|K^d|$ are related by (6). Figure 18 is analogous to figure 17, but with the abscissa converted to the quantity G^d/G_0. Again, it is seen that agreement between the proposed model and the experimental results is good. The deviation of the experimental points from the curve is somewhat more pronounced than in figure 17 since the energy release rate G^d depends on the second power of $|K^d|$.

Similar results were obtained when analysing the PMMA–aluminium test shown in figure 5. Figure 19 is a graphical representation of (15) along with the experimental data points for this test. The normalization point used here is the one corresponding to $v_0 = 600\ \text{m s}^{-1}$. Once again, agreement seems very good, reinforcing the validity of the proposed criterion by using a different material system.

All results shown above were based on the application of the proposed criterion at a distance of 2 mm behind the propagating crack tip. Because of the nature of the interfacial stress and displacement fields predicted by linear elasticity, the relative amounts of opening and shearing displacement behind the crack tip (displacement mixity) varies with distance from it. Therefore it is essential to make all comparisons at the same distance behind the tip. If we were to use a different distance behind the crack tip the numerical results would change. However, our conclusions would still hold as long as all comparisons were made at that one fixed distance.

(*b*) *Discussion and implications of proposed fracture criterion*

In the previous section it was seen that a crack propagating dynamically along a bimaterial interface did so while maintaining the opening and shearing displacements

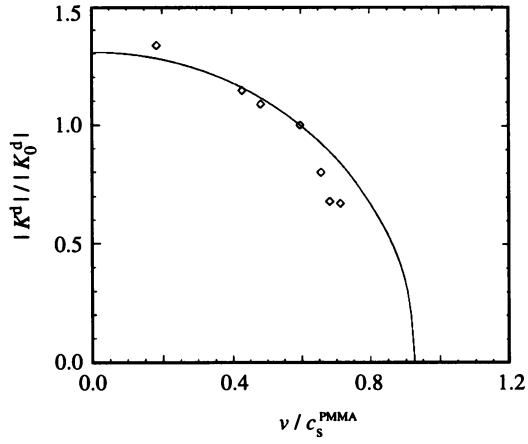

Figure 19. Comparison of normalized stress intensity factor from a PMMA–aluminium drop-weight tower experiment with the prediction of constant crack profile growth.

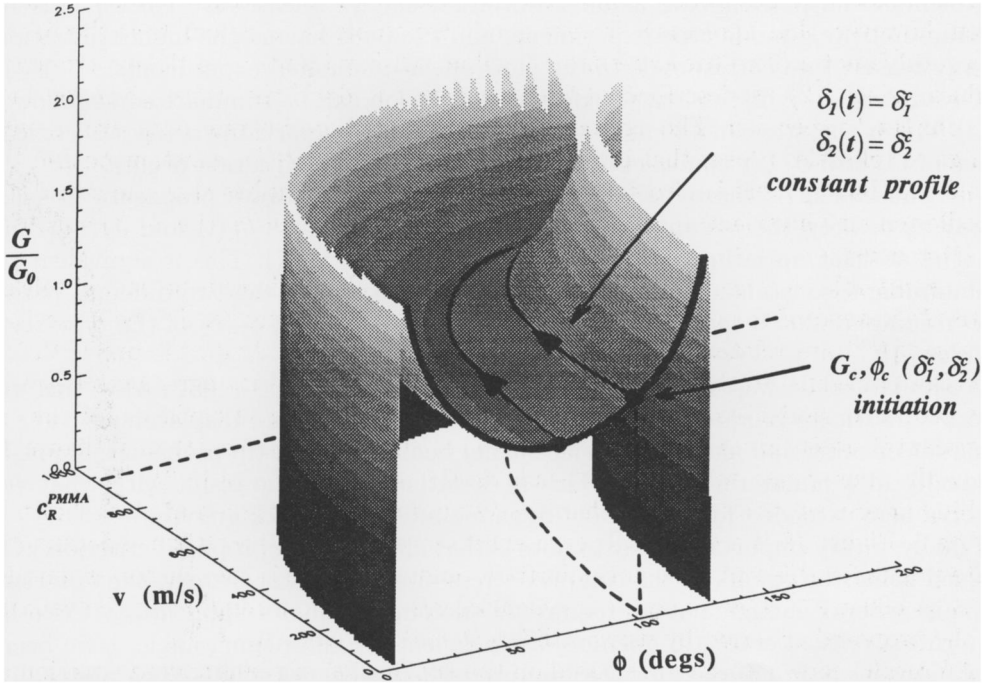

Figure 20. (G^d, v, ϕ) surface for the quantity $\delta_2(t)|_{r=a} = \text{const}$. Crack paths corresponding to constant crack profile are superposed.

at a certain point behind its tip constant. This fact was used to formulate a dynamic propagation criterion that essentially says that the crack face profile remains the same during propagation. What controls the exact crack face profile, or equivalently the constants c_1 and c_2 in (12) and (13), are the precise conditions at crack initiation. This is deduced by the fact that the relation between v and ϕ is such that ϕ remains approximately constant for low v, as exhibited by the two vertical stems in figure 15. Of course, this is also physically based since we do not expect material inertia to become important until substantial crack growth speeds are reached.

An alternative way of viewing the proposed criterion would be as a relation between the energy release rate G^{d}, mixity ϕ and crack speed v. For $v = 0\,\mathrm{m\,s^{-1}}$ this relation should reduce to the widely accepted crack initiation criterion proposed by Liechti (figure 1). To visualize the proposed dynamic crack growth criterion in a three-dimensional G^{d}, ϕ, v space, we plot the surface representing the condition $\delta_2|_{r=a} = C_2$ in figure 20. Recall that points on this surface only satisfy one part of the proposed criterion. If $v = 0\,\mathrm{m\,s^{-1}}$, it is seen from figure 20 that the surface reduces to a '∪'-shaped dependence between G^{d} and ϕ of the type shown in figure 1. Such a '∪'-shaped curve constitutes the initiation condition for a stationary crack loaded dynamically. By requiring the second part of the criterion to be satisfied (i.e. $\delta_1/\delta_2|_{r=a} = C_1$), particular paths on the surface $\delta_2|_{r=a} = C_2$ are traced. This path selection is schematically illustrated in figure 20. Different impact velocities and geometries would cause initiation at a different point, and the curve followed during crack growth would be different, but would still lay on the surface $\delta_2|_{r=a} = C_2$. The two paths shown in figure 20 correspond to the two different regimes of crack propagation of the type observed in the PMMA–steel drop-weight and gas gun experiments. The path having a lower initiation energy release-rate corresponds to the more opening-mode type experiments and the path having the higher initiation energy release-rate corresponds to the more shear-dominated experiments.

Given the above discussion, the proposed criterion can be summarized as follows.

(i) When the stress field surrounding the stationary crack tip reaches a critical value of G_{c} and ϕ_{c} (or equivalently δ_1^c and δ_2^c) then crack initiation occurs.

(ii) Subsequently, the dynamically growing crack will always propagate in such a way as to keep the instantaneous crack-face displacements $\delta_1(t)$ and $\delta_2(t)$ (constant t) at their initiation values (i.e. $\delta_1(t) = \delta_1^c$, $\delta_2(t) = \delta_2^c$). This is equivalent to maintaining a constant crack-face profile. The projection of the two different paths shown in figure 20 on the v, ϕ plane are contours of constant δ_1/δ_2 of the type seen in figure 15.

A similar result was seen in the work of Liechti & Knauss (1982*a*, *b*). Using an interferometric technique, they observed a constant vectorial displacement (i.e. a constant opening and shearing displacement) behind a crack tip propagating quasi-statically in a bimaterial system. This is essentially the same result with what we observe here extended for the case of dynamic interfacial crack growth.

Finally, a very important point to note is that although the proposed criterion was derived using the results of the complex stress-intensity factor history, the criterion itself is general enough not to require K^{d}-dominance in its application. Criteria requiring a critical crack-tip opening displacement, or an opening angle, have been used extensively in the past for the fracture of homogeneous solids. Such physically based criteria have been seen to be equivalent with initiation/growth criteria based on K_{I} or J_{I} in situations where K, J-dominance was assured. However, these physically based criteria have also been observed to be valid in instances when K_{I} or J_{I} cannot attain a physical meaning (e.g. growth in elastic–plastic materials). We therefore believe that the proposed criterion for dynamic interfacial crack growth based on both opening and shearing displacements behind the crack-tip (crack profile) may be valid in a wide array of cases as well; even if a K^{d}-dominant region cannot be found.

5. Concluding remarks

The primary objective of the current study was to obtain a physically motivated and accurate criterion that governs subsonic dynamic interfacial fracture in bimaterial combinations with large mechanical property mismatch. To this end, a sequence of impact tests were performed on various loading configurations of PMMA–steel and aluminium bimaterial systems. It was experimentally observed that the opening and shearing displacements at a given distance behind the propagating crack tip (crack-face profile) remained constant throughout propagation and equal to their initiation values. This observation forms the basis for the proposed dynamic fracture criterion for subsonic interfacial separation.

The support of ONR Grant N00014-90-J-1340 and NSF Grant MSS-9024838 is gratefully appreciated.

References

Atkinson, C. 1977 Dynamic crack problems in dissimilar media. In: *Mechanics of fracture 4: elastodynamic crack problems* (ed. G. C. Sih), pp. 213–248. Leyden: Noorhoff.

Brock, L. M. & Achenbach, J. D. 1973 Extension of an interface flaw under the influence of transient waves. *Int. J. Solids Struct.* **9**, 53–67.

Deng, X. 1993 General crack-tip fields for stationary and steadily growing interface cracks in anisotropic bimaterials. *J. appl. Mech.* **60**, 183–189.

Freund, L. B. 1990 *Dynamic fracture mechanics.* Cambridge University Press.

Geubelle, P. H. & Knauss, W. G. 1994*a* Finite strains at the tip of a crack in a sheet of hyperelastic material. II. Special bimaterial cases. *J. Elast.* **35**, 99–137.

Geubelle, P. H. & Knauss, W. G. 1994*b* Finite strains at the tip of a crack in a sheet of hyperelastic material. III. General bimaterial case. *J. Elast.* **35**, 139–174.

Goldshtein, R. V. 1967 On surface waves in joined elastic materials and their relation to crack propagation along the junction. *Appl. Math. Mech.* **31**, 496–502.

Kanninen, M. F. & Popelar, C. H. 1985 *Advanced fracture mechanics.* Oxford University Press.

Knowles, J. K. & Sternberg, E. 1983 Large deformations near a tip of an interface crack between two Neo-Hookean sheets. *J. Elast* **13**, 257–293.

Lambros, J. & Rosakis, A. J. 1995 Transonic crack growth in bimaterials. I. Experimental observations. *J. Mech. Phys. Solids* **43**, 169–188.

Lee, Y. J. & Rosakis, A. J. 1993 Interfacial cracks in plates: a three-dimensional numerical investigation. *Int. J. Solids Struct.* **30**, 3139–3158.

Lee, Y. J., Lambros, J. & Rosakis, A. J. 1995 Analysis of coherent gradient sensing (CGS) by Fourier optics. *Optics Lasers Engng.* (In the press.)

Liechti, K. M. & Chai, Y. S. 1991 Biaxial loading experiments for determining interfacial fracture-toughness. *J. appl Mech.* **58**, 680–687.

Liechti, K. M. & Knauss, W. G. 1982*a* Crack propagation at material interfaces. I. Experimental technique to determine crack profiles. *Exper. Mech.* **22**, 262–269.

Liechti, K. M. & Knauss, W. G. 1982*b* Crack propagation at material interfaces. II. Experiments on mode interaction. *Exper. Mech.* **22**, 383–391.

Liu, C., Lambros, J. & Rosakis, A. J. 1993 Highly transient elastodynamic crack growth in a bimaterial interface: higher order asymptotic analysis and experiments. *J. Mech. Phys. Solids* **41**, 1887–1954.

Rice, J. R. 1988 Elastic fracture mechanics concepts for interfacial cracks. *J. appl. Mech.* **55**, 98–103.

Rosakis, A. J. 1993 Two optical techniques sensitive to gradients of optical path difference: the method of caustics and the coherent gradient sensor (CGS). In *Experimental techniques in fracture* (ed. J. Epstein), pp. 327–425. VCH Publishers Inc.

Shih, C. F. 1991 cracks on bimaterial interfaces: elasticity and plasticity aspects. *Mater. Sci. Engng* A **143**, 77–90.

Shih, C. F. & Asaro, R. J. 1988 Elastic–plastic analysis of cracks on bimaterial interfaces. I. Small-scale yielding. *J. appl. Mech.* **55**, 299–316.

Shih, C. F. & Asaro, R. J. 1989 Elastic–plastic analysis of cracks on bimaterial interfaces. II. Structure of small scale yielding fields. *J. appl. Mech.* **56**, 763–779.

Shih, C. F., Asaro, R. J. & O'Dowd, N. P. 1991 Elastic–plastic analysis of cracks on bimaterial interfaces. III. Large-scale yielding. *J. appl. Mech.* **58**, 450.

Tippur, H. K., Krishnaswamy, S. & Rosakis, A. J. 1991 Optical mapping of crack-tip deformations using the method of transmission and reflection coherent gradient sensing: a study of crack-tip k-dominance. *Int. J. Fract.* **52**, 91–117.

Tippur, H. V. 1992 Coherent gradient sensing: a Fourier optics analysis and applications to fracture. *Appl. Opt.* **31**, 4428–4439.

Tippur, H. V., Krishnaswamy, S. & Rosakis, A. J. 1991 A coherent gradient sensor for crack-tip measurements: analysis and experimental results. *Int. J. Fract.* **48**, 193–204.

Tippur, H. V. & Rosakis, A. J. 1991 Quasi-static and dynamic crack growth along bimaterial interfaces: a note on crack-tip field measurements using coherent gradient sensing. *Exper. Mech.* **31**, 243–251.

Williams, M. L. 1959 The stresses around a fault or crack in dissimilar media. *Bull. Seismol. Soc. Am.* **49**, 199–204.

Willis, J. R. 1971 Fracture mechanics of interfacial cracks. *J. Mech. Phys. Solids* **19**, 353–368.

Willis, J. R. 1973 Self-similar problems in elastodynamics. *Phil. Trans. R. Soc. Lond.* A **274**, 435–491.

Yang, W., Suo, Z. & Shih, C. F. 1991 Mechanics of dynamic debonding. *Proc. R. Soc. Lond.* A **433**, 679–697.

Received 5 August 1994; revised 7 February 1995; accepted 11 April 1995